Nuclear Science and Techniques (2024) 35:179
https://doi.org/10.1007/s41365-024-01521-2

Cable coupling response in metal cavity under X-ray irradiation

Mao-Xing Zhang[1,3] · Lan-Feng Yuan[1,3] · Cui Meng[2] · Yi-Nong Liu[1,3]

Received: 30 December 2023 / Revised: 29 January 2024 / Accepted: 19 February 2024 / Published online: 27 September 2024

Abstract

This study investigates the coupling response of cables inside a metal cavity under X-ray irradiation using the finite-difference time-domain method, particle simulation method, and transmission-line equation to solve the electromagnetic field inside the cavity and load voltage at the cable terminal under X-ray excitation. The results show that under a strong ionizing radiation environment of 1 J/cm^2, a strong electromagnetic environment is generated inside the cavity. The cable shielding layer terminal couples a voltage of 15.32 V, whereas the core wire terminal couples a voltage of 0.31 V. Under strong X-ray irradiation, the metal cavity not only fails to provide electromagnetic shielding, but also introduces new electromagnetic interference. This study also provides a method for reducing the number of emitted electrons by adding low-Z materials, which can effectively reduce the coupled electric field and voltage.

Keywords Ionizing radiation · Metal cavity · System-generated electromagnetic pulse · Transmission-line model

1 Introduction

When electronic devices are exposed to strong electromagnetic radiation, an electromagnetic coupling response occurs, which may affect the normal operation of the device. A simple and effective shielding method involves placing the device inside a metal cavity, which shields the external electromagnetic field [1, 2] and reduces coupling interference; this is the reason why some devices have metal shells. However, if electronic devices are simultaneously exposed to ionizing radiation (such as inside the target chamber of a laser inertial confinement fusion (ICF) device, with an X-ray fluence of up to 1 J/cm^2) [3], the metal cavity itself will interact with the radiation, causing photoelectric and Compton scattering effects and generating photoelectrons. The photoelectrons emitted inside the cavity excite the electromagnetic field, as shown in Fig. 1. This phenomenon is called the cavity system-generated electromagnetic pulse (SGEMP) [4–7] and may cause new coupling interference to the equipment inside the cavity.

Numerous studies have reported on the simulation and experimentation of the cavity SGEMP [7–12], including studies on the coupling of the cavity SGEMP with intracavity equipment. In 1980, Beers established a simple model for the coupling on a cable caused by a cavity SGEMP [9], but they assumed that the time-domain waveforms of the electric and magnetic fields inside the cavity were derivatives of the X-ray time-domain waveforms, ignoring factors such as the resonance inside the cavity [9]. In 1982, Seidler established an equivalent-circuit model for the coupling of the cavity SGEMP of a component box to a printed circuit board (PCB) and classified and discussed the capacitive coupling generated by the electric field and inductive coupling generated by the magnetic field [10]. In 2022, Chen calculated the coupling response of the cavity SGEMP to PCB interconnects using the extended finite-difference time-domain (FDTD) method, considering various printed interconnect structures and loads [11].

In this study, the three-dimensional FDTD method is combined with the transmission-line equation to study the coupling effect of the cavity SGEMP on a shielded cable inside the cavity. The calculation methods for the cavity SGEMP and field-line coupling are described in Sects. 2 and 3, respectively. The code verification is presented in

✉ Cui Meng
mengcui@zju.edu.cn

[1] Department of Engineering Physics, Tsinghua University, Beijing 100084, China

[2] College of Electrical Engineering, Zhejiang University, Hangzhou 310007, China

[3] Laboratory of Particle and Radiation Imaging, Ministry of Education, Beijing 100084, China

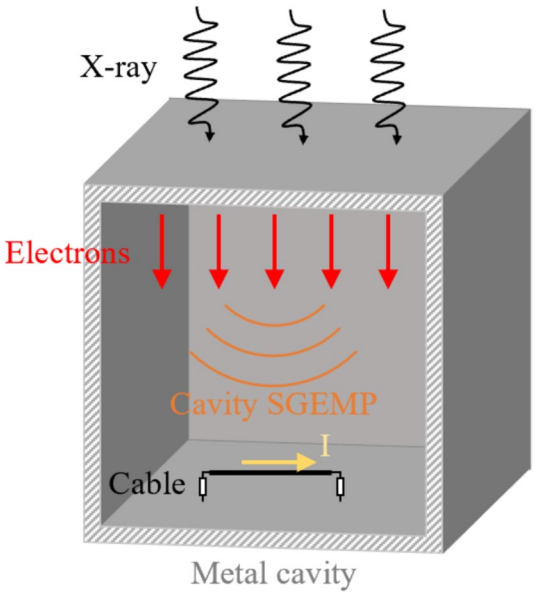

Fig. 1 (Color online) Schematic of cavity SGEMP coupling

Sect. 4. In Sect. 5, the coupling response of a shielded cable inside a metal cavity under X-ray irradiation is calculated, and the coupling law is analyzed. Finally, the conclusions are presented in Sect. 6.

2 Calculation method for cavity SGEMP

The calculation of the cavity SGEMP can be divided into two parts: the interaction between the X-rays and cavity wall, which causes electron emission, and the emission of electrons, which excites the electromagnetic pulses. For the first part, we used the Monte Carlo software Geant4 to simulate the electron yield caused by X-rays [13]. For the second part, we used a simulation program independently developed by our research group to calculate the cavity SGEMP generated by electron motion.

The high-speed motion of the emitting electrons forms a spatial current density that serves as the current source term in Maxwell's equations for exciting the electromagnetic field. Simultaneously, electromagnetic fields constrain the motion of charged particles, affecting the speed and position of electrons through electric- and magnetic-field forces. Therefore, unlike traditional computational electromagnetic problems, the emission of electron-excited electromagnetic pulses is a self-consistent process of electron–electromagnetic field interaction, and the interaction between electromagnetic pulses and excitation sources requires the use of electromagnetic particle simulation algorithms.

In most physical problems, the number of emitted electrons is large; therefore, we use the particle in cell (PIC) simulation method to solve the particle motion parameters and establish a macroparticle model to reduce computational memory. To calculate the time-domain electromagnetic field, the FDTD method is one of the most widely used numerical algorithms, and its Yee mesh is advantageous when combined with macroparticle models. Therefore, this study adopts an algorithm that combines FDTD and PIC to calculate the cavity SGEMP.

The following sections introduce the algorithms used in the simulation.

2.1 Finite-difference time-domain method

The FDTD method requires spatial and temporal discretizations of the electric- and magnetic-field components in the Yee grid to calculate the temporal and spatial variations in the electromagnetic field, respectively [14]. The Maxwell rotation equation system in a vacuum is as follows [15]:

$$\begin{cases} \nabla \times \vec{E} = -\frac{\partial \vec{B}}{\partial t} \\ \nabla \times \vec{H} = \frac{\partial \vec{D}}{\partial t} + \vec{J} \end{cases} \tag{1}$$

where $\vec{E}$ is the electric-field intensity vector, in V/m, $\vec{D}$ is the electric-displacement vector, expressed in C/m^2, $\vec{H}$ is the magnetic-field intensity vector, measured in V/m^2, $\vec{B}$ is the magnetic induction intensity vector, in units of Wb/m^2, and $\vec{J}$ is the current-density vector, measured in A/m^2. In this study, the current density is caused by photoelectron emission.

In an isotropic medium, we have:

$$\begin{cases} \vec{D} = \epsilon \vec{E} \\ \vec{B} = \mu \vec{H} \end{cases} \tag{2}$$

where ϵ is the dielectric constant of the medium, in F/m, and μ is the magnetic permeability coefficient, in H/m. This study assumes vacuum conditions inside the metal cavity; therefore, $\epsilon = \epsilon_0 = 8.854 \times 10^{-12}$ F/m and $\mu = \mu_0 = 4\pi \times 10^{-7}$ H/m.

This study establishes an FDTD model using a three-dimensional Cartesian coordinate system. By substituting the components of the electric and magnetic fields into Eq. (1), we obtain the following scalar equation:

$$\begin{cases} \epsilon \frac{\partial E_x}{\partial t} = \frac{\partial H_z}{\partial y} - \frac{\partial H_y}{\partial z} - J_x \\ \epsilon \frac{\partial E_y}{\partial t} = \frac{\partial H_x}{\partial z} - \frac{\partial H_z}{\partial x} - J_y \\ \epsilon \frac{\partial E_z}{\partial t} = \frac{\partial H_y}{\partial x} - \frac{\partial H_x}{\partial y} - J_z \\ \mu \frac{\partial H_x}{\partial t} = \frac{\partial E_y}{\partial z} - \frac{\partial E_z}{\partial y} \\ \mu \frac{\partial H_y}{\partial t} = \frac{\partial E_z}{\partial x} - \frac{\partial E_x}{\partial z} \\ \mu \frac{\partial H_z}{\partial t} = \frac{\partial E_x}{\partial y} - \frac{\partial E_y}{\partial x} \end{cases} \tag{3}$$

Taking the first formula of Eq. (3) as an example, performing the center difference can yield the FDTD formula in a three-dimensional Cartesian coordinate system as follows:

$$\begin{cases} E_x^{n+1}\left(i+\frac{1}{2},j,k\right) = E_x^{n}\left(i+\frac{1}{2},j,k\right) + \frac{\Delta t}{\epsilon}\cdot\left[\frac{H_z^{n+1}\left(i+\frac{1}{2},j+\frac{1}{2},k\right)-H_z^{n+1}\left(i+\frac{1}{2},j-\frac{1}{2},k\right)}{\Delta y}\right. \\ \left. -\frac{H_y^{n+1}\left(i+\frac{1}{2},j,k+\frac{1}{2}\right)-H_y^{n+1}\left(i+\frac{1}{2},j,k-\frac{1}{2}\right)}{\Delta z} - J_x^{n+\frac{1}{2}}\left(i+\frac{1}{2},j,k\right)\right] \end{cases} \tag{4}$$

Similarly, the other components of the FDTD formulae in Eq. (3) can be obtained.

Owing to the introduction of discrete errors because of the central difference, the time and spatial step sizes must satisfy the Courant stability condition [16]:

$$c\Delta t \le \frac{1}{\sqrt{\frac{1}{(\Delta x)^2}+\frac{1}{(\Delta y)^2}+\frac{1}{(\Delta z)^2}}}. \tag{5}$$

2.2 Particle in cell method

After establishing the FDTD formula in Sect. 2.1, the key to solving for the electromagnetic field lies in the current density $\vec{J}$. The PIC method was used to calculate the motion parameters of the electrons to solve the current density $\vec{J}$ [17]. Because of the large number of emitted electrons, this study equates some electrons with similar positions, velocities, and other characteristics to a macroparticle and completes the simulation of actual physical processes containing a large number of electrons by simulating a small number of macroparticles.

The relationship between the position vector $\vec{r}$ of the macroparticles and time is

$$\frac{\mathrm{d}\vec{r}}{\mathrm{d}t} = \vec{v}. \tag{6}$$

In the three-dimensional Cartesian coordinate system, we perform central difference processing on the above equation and obtain the iterative equation as follows:

$$\begin{cases} x^{n+1} = x^n + v_x^{n+\frac{1}{2}}\Delta t \\ y^{n+1} = y^n + v_y^{n+\frac{1}{2}}\Delta t \\ z^{n+1} = z^n + v_z^{n+\frac{1}{2}}\Delta t \end{cases} \tag{7}$$

Electron motion is mainly influenced by electromagnetic forces, and relativistic effects must be considered for high-velocity electrons. Therefore, the momentum equation is

$$\frac{\mathrm{d}(\gamma m_0\vec{v})}{\mathrm{d}t} = q\left(\vec{E}+\vec{v}\times\vec{B}\right), \tag{8}$$

where m_0 is the stationary mass of the macroparticle, and $\gamma = \frac{1}{\sqrt{1-\frac{v^2}{c^2}}}$ is the Lorentz factor.

The effect of an electromagnetic field on electrons is decomposed into half-acceleration caused by two electric fields and rotation caused by one magnetic field such that $\vec{u} = \gamma\vec{v}$. By centrally differencing the momentum equation, we obtain

$$\vec{u}^{n+\frac{1}{2}} = \left(\vec{u}^{n-\frac{1}{2}} + \frac{q\vec{E}^n}{m_0}\frac{\Delta t}{2}\right) + \frac{q\left(\vec{u}^{n+\frac{1}{2}}+\vec{u}^{n-\frac{1}{2}}\right)\times\vec{B}^n}{2\gamma^n m_0}\cdot\Delta t + \frac{q\vec{E}^n}{m_0}\frac{\Delta t}{2}. \tag{9}$$

The particle velocity can be iterated via calculation, thereby achieving iterative updates of the particle position.

To determine the current density, the charge conservation equation is $\nabla\cdot\vec{J} = -\frac{\rho}{t}$. The differential form in the three-dimensional Cartesian coordinate system is

$$\frac{\partial J_x}{\partial x} + \frac{\partial J_y}{\partial y} + \frac{\partial J_z}{\partial z} = -\frac{\partial \rho}{\partial t}. \tag{10}$$

Therefore, on grid nodes (i, j, k), the following can be obtained:

$$\frac{J_x^{n+\frac{1}{2}}\left(x+\frac{1}{2},y,z\right)}{\Delta x} + \frac{J_y^{n+\frac{1}{2}}\left(x,y+\frac{1}{2},z\right)}{\Delta x} + \frac{J_z^{n+\frac{1}{2}}\left(x,y,z+\frac{1}{2}\right)}{\Delta x} = -\frac{\rho^{n+1}(x,y,z)-\rho^n(x,y,z)}{\Delta t}. \tag{11}$$

Performing the same operation on grid nodes $(i,j+1,k)$, $(i,j,k+1)$, and $(i,j+1,k+1)$, and adding the four equations yields

$$J_x\left(i+\frac{1}{2},j,k\right) + J_x\left(i+\frac{1}{2},j+1,k+1\right) + J_x\left(i+\frac{1}{2},j,k+1\right) + J_x\left(i+\frac{1}{2},j+1,k\right) = \rho_0\frac{x^{n+1}(p)-x^n(p)}{\Delta t} = J_x. \tag{12}$$

Similarly, the values of each current-density component can be obtained, and the variation in the cavity SGEMP over time can be solved by combining it with the FDTD method mentioned earlier. Many studies have previously combined the FDTD method with the PIC method. Chen et al.

proposed the conformal PIC method to simulate the cavity SGEMP [18, 19] using the UNIPIC code [20, 21]. The most important features of the conformal method are that the code can handle complex geometric structures without staircased approximation and can simulate the electromagnetic fields generated from electrons distributed at different angles.

3 Calculation method for field-line coupling

3.1 Transmission-line model of shielded cable under external excitation

After obtaining the electromagnetic environment inside the cavity from Sect. 2, the coupling response of the cable inside the cavity can be solved as follows.

The transmission-line model is often used to analyze the field-line coupling problem under electromagnetic pulse excitation. Shielded cables can be considered as two transmission-line systems [22]: The shield of the cable and external circuit (external wire or ground) form an external transmission-line system, and the shield and inner conductor form an internal transmission-line system, as shown in Fig. 2. The connection between these two transmission-line systems can be described by the transfer impedance and admittance of the shielded cables.

The field-line coupling problem has been studied by many researchers, and commonly used models include the Agrawal, Taylor, and Rachidi models [23–25]. This study used the Agrawal model to study the response of an external transmission-line system under an external-field excitation. The model assumes that the coupling between the external electromagnetic field and transmission line can be considered an electromagnetic scattering phenomenon, and the coupling effect of the electromagnetic field on the cable is equivalent to the combined voltage source at both ends and the distributed voltage source on the line.

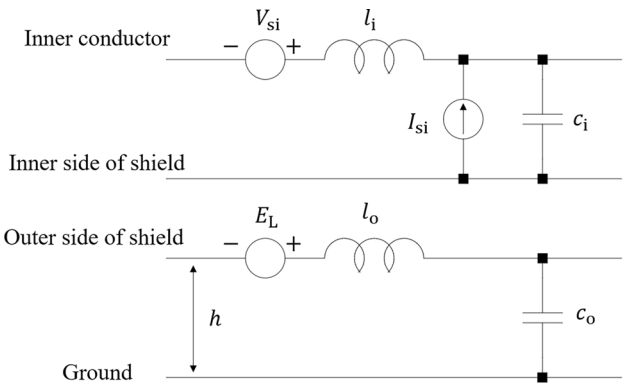

Fig. 2 Unit-length circuit diagram for cable shield and ground and cable shield and inner conductor

Assuming that the cable is located at a height above the reference ground plane, the equation set for the transmission line of the external system is given as follows:

$$\begin{cases} \frac{\partial V_{os}(x,t)}{\partial x} + l_o \frac{\partial I_o(x,t)}{\partial t} = E_L \\ \frac{\partial I_o(x,t)}{\partial x} + c_o \frac{\partial V_{os}(x,t)}{\partial t} = 0 \end{cases} \tag{13}$$

where $V_{os}(x,t)$ and $I_o(x,t)$ represent the scattering voltage and current of the external system, respectively, l_o represents the distributed inductance, c_o is the distributed capacitance, and the distributed voltage source $E_L = E_x^{ex}(x,h,t)$ represents the polarization of the electric field in the x direction at position x and height h from the ground at time t. The boundary conditions at both ends of the cable shield are as follows:

$$\begin{cases} V_{os}(0,t) = -R_{oS} I_o(0,t) + V_S \\ V_{os}(L,t) = R_{oL} I_o(L,t) + V_L \end{cases} \tag{14}$$

where R_{oS} and R_{oL} represent the grounding load values at the left and right ends of the cable shield, respectively. V_S and V_L represent the voltage sources formed by the excitation of the electric field at the left and right terminals of the transmission line, respectively, which can be expressed as follows:

$$\begin{cases} V_S = \int_0^h E_z^{ex}(0,z,t)\mathrm{d}z \\ V_L = \int_0^h E_z^{ex}(L,z,t)\mathrm{d}z \end{cases} \tag{15}$$

where $E_z^{ex}(x,z,t)$ represents the z-direction electric-field intensity at position x and height h above the ground at time t.

The relationship between the scattering voltage $V_{os}(x,t)$ and total voltage $V_o(x,t)$ of the shield is

$$V_o(x,t) = V_{os}(x,t) + V_{oi}(x,t), \tag{16}$$

where $V_{oi}(x,t) = -\int_0^h E_z^{ex}(x,z,t)\mathrm{d}z$.

After the current and voltage responses of the external shield are obtained, the transmission-line equation for the internal system of the shielded cable is established as follows:

$$\begin{cases} \frac{\partial V_i(x,t)}{\partial x} + l_i \frac{\partial I_i(x,t)}{\partial t} = V_{si}(x,t) \\ \frac{\partial I_i(x,t)}{\partial x} + c_i \frac{\partial V_i(x,t)}{\partial t} = I_{si}(x,t) \end{cases} \tag{17}$$

where $V_i(x,t)$ and $I_i(x,t)$ represent the voltage and current of the internal transmission-line system, respectively, l_i represents the distributed inductance, c_i represents the distributed capacitance, and $V_{si}(x,t)$ and $I_{si}(x,t)$ are the distributed excitation sources of the internal transmission-line system, expressed as follows:

$$\begin{cases} V_{si}(x,t) = Z_t(t) I_o(x,t) \\ I_{si}(x,t) = -Y_t(t) V_o(x,t) \end{cases} \tag{18}$$

where $Z_t(t)$ and $Y_t(t)$ are the transfer impedance and transfer admittance of the shielded cable, respectively. The commonly used simple model is [18]

$$\begin{cases} Z_t(t) = R_{dc} + j\omega L_t \\ Y_t(t) = j\omega C_t \end{cases} \tag{19}$$

where R_{dc} denotes the transfer resistance, ω is the angular frequency, L_t is the transfer inductance, and C_t is the transfer admittance. This model assumes that R_{dc} is constant, independent of the frequency, and larger than the actual value; however, it satisfies the worst-case estimation [26].

Based on the above equations, we conclude that

$$\begin{cases} \frac{\partial V_i(x,t)}{\partial x} + l_i \frac{\partial I_i(x,t)}{\partial t} = R_{dc} I_o(x,t) + L_t \frac{\partial I_o(x,t)}{\partial x} \\ \frac{\partial I_i(x,t)}{\partial x} + c_i \frac{\partial V_i(x,t)}{\partial t} = -C_t \frac{\partial V_o(x,t)}{\partial x} \end{cases} \tag{20}$$

3.2 Differential approximation of cable transmission-line equations

Using the one-dimensional FDTD method to solve the transmission-line equation, the cable is first discretized and divided into *NDZ* segments, with each segment having a length of Δz. Similarly, the entire solution time is divided into *NDT* segments, with each segment being Δt [27].

The voltage at point $NDZ + 1$ is interleaved with the current at point *NDZ* for a solution with a spatial interval $\Delta z/2$ between each voltage point and adjacent current points. Simultaneously, the time points should also be interwoven with a time interval of $\Delta t/2$ between each voltage point and adjacent current points.

For external and internal transmission-line systems, the iterative equation obtained by performing the central difference between the voltage and current is

$$\begin{aligned} I_{o_k}^{n+\frac{3}{2}} = I_{o_k}^{n+\frac{1}{2}} - \frac{\Delta t}{l_o \Delta z}\left(V_{os_{k+1}}^{n+1} - V_{os_k}^{n+1}\right) \\ + \frac{\Delta t}{2l_o}\left(E_{L_{k+1}}^{n+1} + E_{L_k}^{n+1}\right) \end{aligned} \tag{21}$$

$$V_{os_k}^{n+1} = V_{os_k}^{n} - \frac{\Delta t}{c_o \Delta z}\left(I_{o_k}^{n+\frac{1}{2}} - I_{o_{k-1}}^{n+\frac{1}{2}}\right) \tag{22}$$

$$\begin{aligned} I_{i_k}^{n+\frac{3}{2}} = I_{i_k}^{n+\frac{1}{2}} - \frac{\Delta t}{l_i \Delta z}\left(V_{i_{k+1}}^{n+1} - V_{i_k}^{n+1}\right) \\ + \left(R_{dc}\frac{\Delta t}{2l_i} + \frac{L_t}{l_i}\right) I_{o_k}^{n+\frac{3}{2}} + \left(R_{dc}\frac{\Delta t}{2l_i} - \frac{L_t}{l_i}\right) I_{o_k}^{n+\frac{1}{2}} \end{aligned} \tag{23}$$

$$\begin{aligned} V_{i_k}^{n+1} = V_{i_k}^{n} - \frac{\Delta t}{c_i \Delta z}\left(I_{i_k}^{n+\frac{1}{2}} - I_{i_{k-1}}^{n+\frac{1}{2}}\right) \\ - \frac{C_t}{c_i}\left(V_{o_k}^{n+1} - V_{o_k}^{n}\right). \end{aligned} \tag{24}$$

The boundary conditions satisfy the following equations:

$$\begin{aligned} V_{os_1}^{n+1} = \left(1 + c_o R_{oS}\frac{\Delta z}{\Delta t}\right)^{-1}\left[\left(c_o R_{oS}\frac{\Delta z}{\Delta t} - 1\right)V_{os_1}^{n}\right. \\ \left. -2R_{oS} I_{o_1}^{n+\frac{1}{2}} + \left(V_S^{n+1} + V_S^{n}\right)\right] \end{aligned} \tag{25}$$

$$\begin{aligned} V_{os_{NDZ+1}}^{n+1} = \left(1 + c_o R_{oL}\frac{\Delta z}{\Delta t}\right)^{-1}\left[\left(c_o R_{oL}\frac{\Delta z}{\Delta t} - 1\right)\right. \\ \left. V_{os_{NDZ+1}}^{n} + 2R_{oL} I_{o_{NDZ}}^{n+\frac{1}{2}} + \left(V_L^{n+1} + V_L^{n}\right)\right] \end{aligned} \tag{26}$$

$$\begin{aligned} V_{i_1}^{n+1} = \left(1 + c_i R_{oS}\frac{\Delta z}{\Delta t}\right)^{-1}\left[\left(c_i R_{iS}\frac{\Delta z}{\Delta t} - 1\right)V_{i_1}^{n}\right. \\ \left. +2R_{iS} I_{i_1}^{n+\frac{1}{2}} - C_t R_{iS}\frac{\Delta z}{\Delta t}\left(V_{os_1}^{n+1} - V_{os_1}^{n}\right)\right] \end{aligned} \tag{27}$$

$$\begin{aligned} V_{i_{NDZ+1}}^{n+1} = \left(1 + c_i R_{iL}\frac{\Delta z}{\Delta t}\right)^{-1}\left[\left(c_i R_{iL}\frac{\Delta z}{\Delta t} - 1\right)V_{i_{NDZ+1}}^{n}\right. \\ \left. +2R_{iL} I_{i_{NDZ}}^{n+\frac{1}{2}} - C_t R_{iL}\frac{\Delta z}{\Delta t}\left(V_{os_{NDZ+1}}^{n+1} - V_{os_{NDZ+1}}^{n}\right)\right]. \end{aligned} \tag{28}$$

4 Code verification

First, for the cavity SGEMP calculation part of the code, our research group developed a 3D simulation program that was previously reported in [5, 28]; it has good convergence and has been widely recognized. This study will not elaborate on the program further.

The following section introduces the verification of the field-line coupling part of the code. This study adopts the same calculation conditions as those in [29, 30]. An external electromagnetic wave is vertically irradiated on an RG-58 cable located on the ground, and the polarization direction of the electric field is parallel to the direction of the cable placement. The length of the cable is 1 m, and the height h from the ground is 1 cm. The external terminal loads are $R_{oS} = 100\,\Omega$ and $R_{oL} = 150\,\Omega$, and the internal terminal load is $R_{iS} = R_{iL} = 50\,\Omega$.

The incident electromagnetic wave uses the electromagnetic pulses according to the IEC standard, $E(t) = kE_0(e^{-\beta t} - e^{-\alpha t})$, where $k = 1.3$, $E_0 = 50\,\mathrm{kV/m}$, $\alpha = 6 \times 10^8\,\mathrm{s}^{-1}$, $\beta = 4 \times 10^7\,\mathrm{s}^{-1}$.

The outer radius r_{se} of the shielding layer of the RG-58 cable is 1.52 mm, the inner radius $r_{si} = 1.40$ mm, the number of weaving strands $C = 12$, the number of copper wires per strand $N = 9$, the diameter of the metal wire $d = 0.127$ mm, and the weaving angle $\alpha = 27.7°$. The relative dielectric constant ϵ_r of the dielectric inside the cable is 1.85, and the internal characteristic impedance is 50 Ω. The transfer resistance R_{dc} of the cable, transfer inductance L_t, and transfer capacitance C_t can be calculated using the following equations as 14.2 mΩ/m, 1.0 nH/m, and 0.091 pF/m, respectively

$$R_{dc} \approx \frac{4}{\pi d^2 NC\sigma \cos\alpha} \tag{29}$$

$$L_t \approx \begin{cases} \frac{\pi\mu_0}{6C}(1-K_C)^{3/2}\frac{e^2}{E(e)-(1-e^2)K(e)} & (\alpha < 45°) \\ \frac{\pi\mu_0}{6C}(1-K_C)^{3/2}\frac{e^2/\sqrt{1-e^2}}{K(e)-E(e)} & (\alpha > 45°) \end{cases} \tag{30}$$

$$C_t \approx \begin{cases} \frac{\pi C_{out}C_{in}}{3(\epsilon_{out}+\epsilon_{in})C}(1-K_C)^{3/2}\frac{1}{E(e)} & (\alpha < 45°) \\ \frac{\pi C_{out}C_{in}}{3(\epsilon_{out}+\epsilon_{in})C}(1-K_C)^{3/2}\frac{\sqrt{1-e^2}}{E(e)} & (\alpha > 45°) \end{cases} \tag{31}$$

where K_C represents the projection coverage of the braided shielding layer, defined as $K_C = 2F - F^2$, where F represents the filling rate of the woven layer, defined as $F = PNd/\sin\alpha$, and P represents the number of cross sections. $K(e)$ and $E(e)$ represent complete elliptic integral functions of the first and second types, respectively [31].

$$e = \begin{cases} \sqrt{1-\tan^2\alpha} & (\alpha < 45°) \\ \sqrt{1-\cot^2\alpha} & (\alpha > 45°) \end{cases} \tag{32}$$

The Agrawal transmission-line model established in this study is used to calculate the coupling voltage of the external and internal terminal loads, and the results are compared with those obtained using the SPICE model in reference [29]. As shown in Fig. 3, the calculation results are consistent.

5 Calculation and analysis

The calculation model established in this study is shown in Fig. 1. The metal cavity is an aluminum cube shell with a side length of 0.6 m and thickness of 1 mm. We assume that the cable inside the cavity is RG-58 with parameters consistent with those in Sect. 3, that is, a length of 0.2 m and height of 0.1 m from the bottom of the cavity. The terminal loads between the cable shield and cavity are both 1 Ω, and the terminal loads between the cable inner conductor and shield are both 50 Ω. Assuming that the X-ray energy is 10 keV, the fluence is 1 J/cm^2, and the time-domain waveform is a Gaussian pulse with a pulse width of 1 ns, the top surface of the cavity is uniformly irradiated. During the calculation,

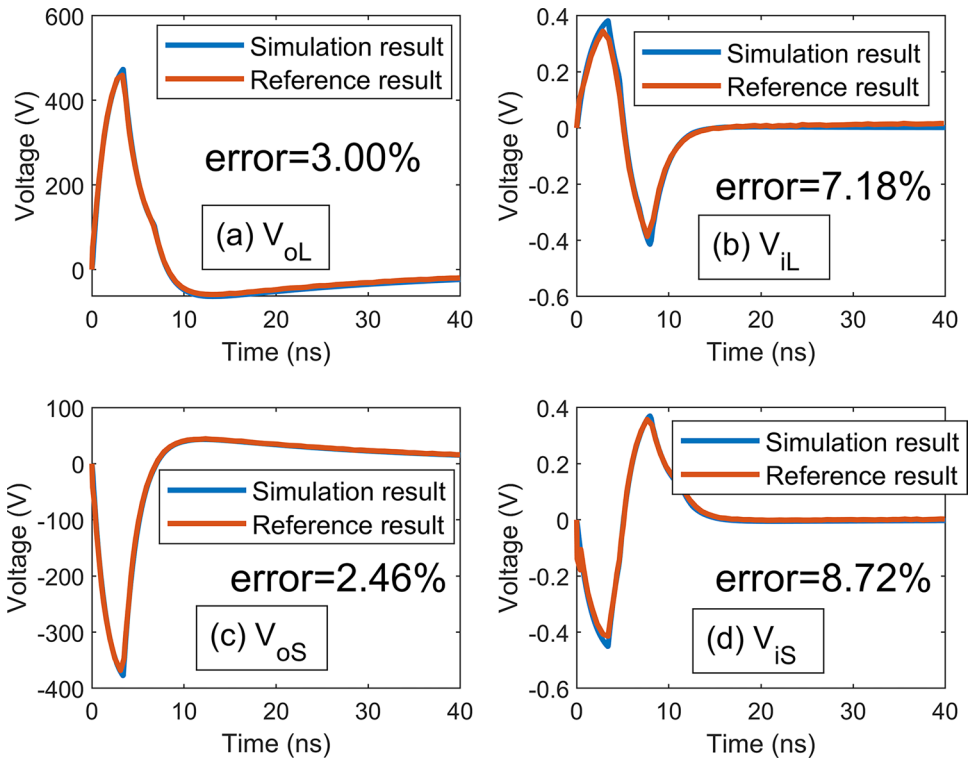

Fig. 3 Comparison between simulation results and literature results. V_{iS} and V_{iL} represent the voltage of the terminal load at the left and right ends of the inner conductor, and V_{oS} and V_{oL} represent the voltage of the terminal load at the left and right ends of the cable shielding, respectively

the internal mesh of the cavity is divided into 1-cm cubic meshes.

Using the Monte Carlo software Geant4, the photoelectron yield generated by 10-keV X-ray irradiation on 1-mm-thick aluminum was calculated to be 1.94×10^{-6}. Therefore, the total number of electrons was calculated as 4.365×10^{12}. Using electrons as the input, the electromagnetic field of each grid node inside the metal cavity and the coupling voltage and current of the cable-terminal loads were calculated.

First, the electric-field strength is analyzed at the location of the cable: the left end, midpoint, and right end of the cable are selected, denoted as points A, B, and C, respectively. The time-domain waveform and spectrum of the vertical electric field E_z and the electric field E_x along the cable at the three node positions of the cable are calculated, as shown in Fig. 4. The amplitude of E_z does not differ significantly at each node. The waveform is basically consistent, and the amplitude is larger than E_x. This is because, under X-ray irradiation, electrons are uniformly emitted from the top surface of the cavity downwards, and the vertical electric-field amplitude is large. The cable is located in the central area, and the distribution of E_z is relatively uniform. The amplitude of E_x varies with position, with the minimum amplitude at the midpoint of the cable and the maximum amplitude at both ends. The polarization directions of the electric field at the ends are opposite because of the symmetry of the cube cavity.

The spectrum shows that E_z has two main resonant frequencies: 350 MHz and 425 MHz. According to Eq. 33 to calculate the resonant frequency of the rectangular cavity, the resonant modes in the 0.6-m cubic cavity are determined to be TM110 (353 MHz) and TM111 (433 MHz). E_x has two main resonant frequencies, 425 MHz and 600 MHz, corresponding to TE111 (433 MHz) and TE112 (612 MHz), respectively. This also indicates that different directions contain different resonant modes [5].

$$f_{nml} = \frac{c}{2\pi\sqrt{\mu_r \epsilon_r}} \sqrt{\left(\frac{m\pi}{a}\right)^2 + \left(\frac{n\pi}{b}\right)^2 + \left(\frac{l\pi}{d}\right)^2}, \tag{33}$$

where mnl represents the resonant mode; a, b, and d represent the length, width, and height of the cavity, respectively; c represents the speed of light; μ_r represents the relative magnetic permeability; and ϵ_r represents the relative dielectric constant.

Subsequently, we calculate and analyze the coupling voltage of the cable-terminal loads, as shown in Fig. 5. The peak amplitude of V_{oL} is 15.32 V, and the peak amplitude of V_{iL} is 0.63 V. The cable shield has good shielding effectiveness, and the metal cavity itself may cause coupling interference to the internal cable under a strong ionizing radiation environment. The spectrum shows that some frequencies in the coupling voltage are the resonant frequencies of the electric field, and higher-frequency harmonics also appear.

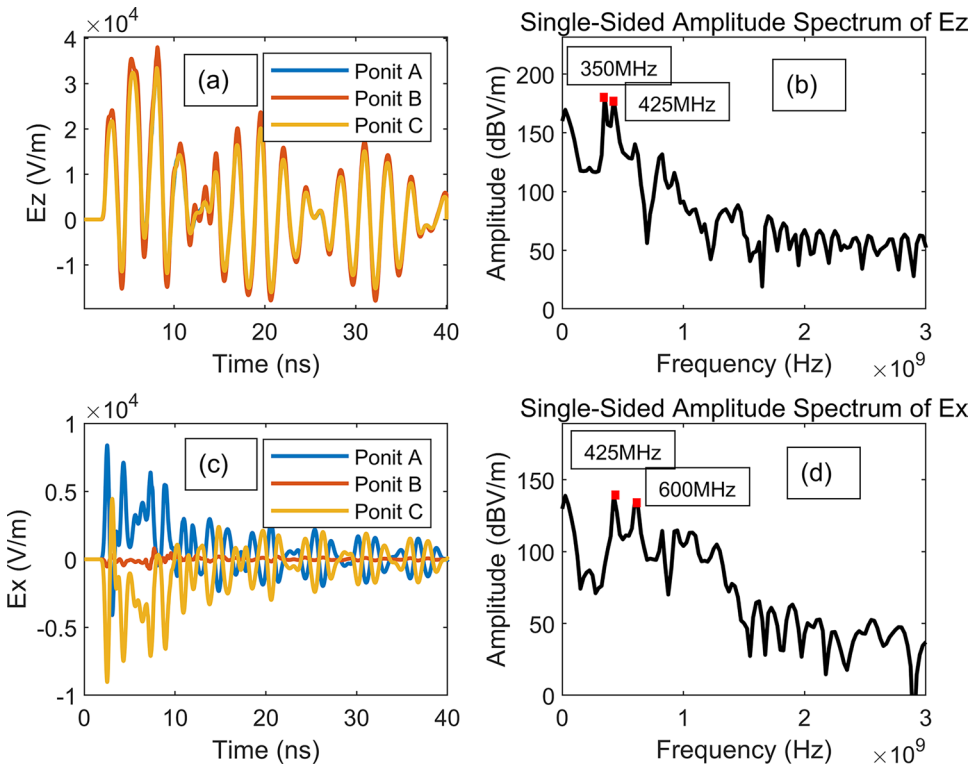

Fig. 4 **a**, **b** The vertical electric-field strength at each node position of the cable. **a** Time-domain waveform and **b** frequency spectrum. **c**, **d** The horizontal electric-field strength at each node position of the cable. **c** Time-domain waveform and **d** frequency spectrum

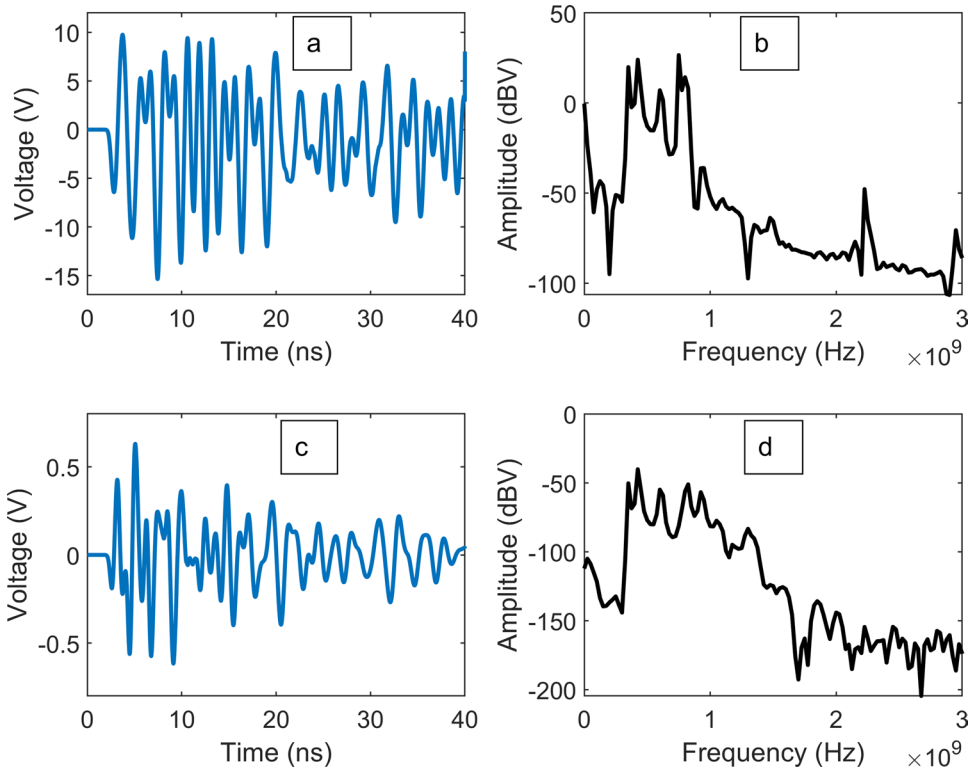

5 **a**, **b** The coupling voltage V_{oL} of the shield terminal load. **a** Time-domain waveform and **b** frequency spectrum. **c**, **d** The coupling voltage V_{iL} of inner conductor terminal load. **c** Time-domain waveform and **d** frequency spectrum

We then calculate the coupling voltage by changing different parameters. In practical applications, the size of the metal cavity is fixed, such as the stripe camera inside the target chamber of the ICF device. In this case, the variable that can be changed is the cable layout inside the metal cavity. Therefore, in this study, the cable length and height from the cavity wall (ground plane) are used as representatives. The source of the cavity SGEMP is the electrons emitted from the cavity wall. If the X-ray intensity, cavity-wall material, and cavity-wall thickness are changed, this will change the number of emitted electrons. Therefore, the effects of different numbers of emitted electrons are simulated in this study.

5.1 Cable length

The cable lengths are set to 0.1 m, 0.2 m, 0.3 m, 0.4 m, and 0.5 m, keeping the other parameters unchanged. The coupling voltage of the inner conductor terminal load is calculated, as shown in Fig. 6a. As the cable length increases, the amplitude of the coupling voltage increases. This is because the external electromagnetic field remains unchanged, and as the cable length increases, the distribution of the voltage sources increases, leading to an increase in the coupling voltage.

Figure 6b shows the relationship between the peak amplitude of the coupling voltage V_{iL} and cable length, and the two are approximately linearly related.

5.2 Cable height

The distances between the cable and the bottom of the cavity are set to 0.05 m, 0.1 m, 0.15 m, 0.2 m, and 0.25 m, while keeping the other parameters unchanged. The calculated coupling voltage of the inner conductor terminal load is shown in Fig. 6c. As the cable height increases, the amplitude of the coupling voltage increases. This is mainly because, as the height increases, the area between the transmission line and the ground as a reference conductor increases, leading to more electromagnetic energy coupling into the transmission line and an increase in the coupling current.

Figure 6d shows the relationship between the peak amplitude of coupling voltage V_{iL} and the height of the cable, and the two are also approximately linearly related.

5.3 Number of emitted electrons

According to the physical model of the cavity SGEMP described in Sect. 2, when the cavity size and the X-ray energy are constant, the number of emitted electrons determines the cavity SGEMP field strength amplitude. Therefore, we set the number of emitted electrons to 1×10^{10}, 1×10^{11}, 1×10^{12}, 4.365×10^{12}, and 1×10^{13}, while keeping other parameters unchanged. The calculated E_z field strength and coupling voltage V_{iL} are shown in Fig. 7. As the number of emitted electrons increases, both the field strength and

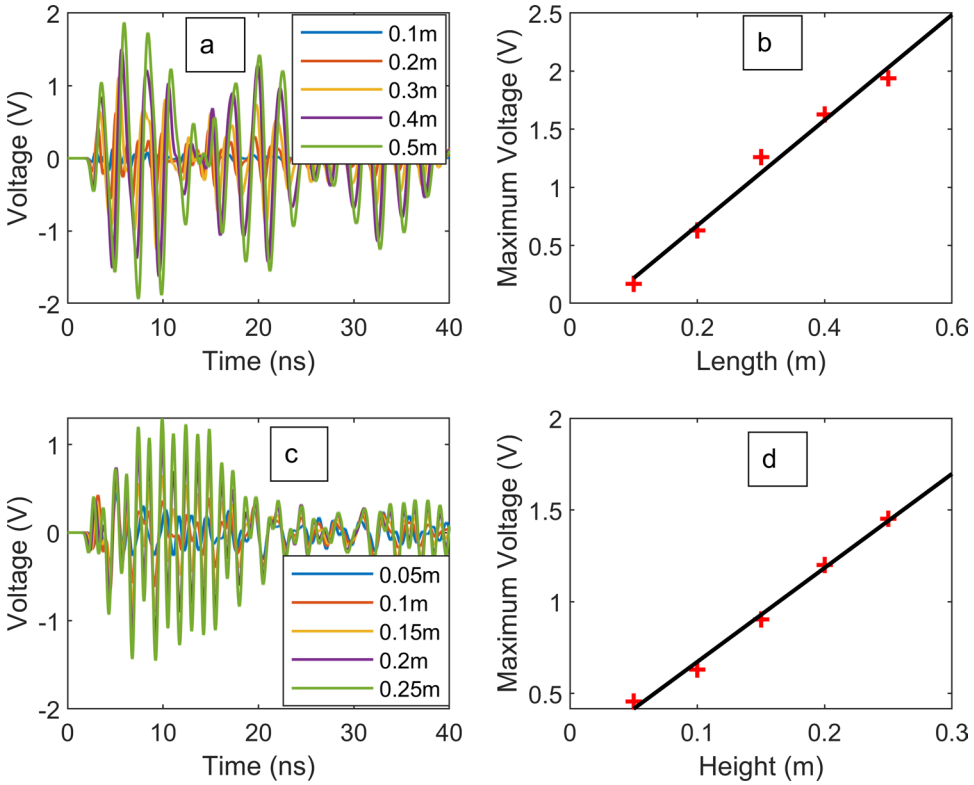

Fig. 6 **a** Time-domain waveform of coupling voltage V_{iL} for cables of different lengths. **b** Relationship between peak amplitude of coupling voltage V_{iL} and length. **c** Time-domain waveform of coupling voltage V_{iL} for cables of different heights. **d** Relationship between peak amplitude of coupling voltage V_{iL} and height

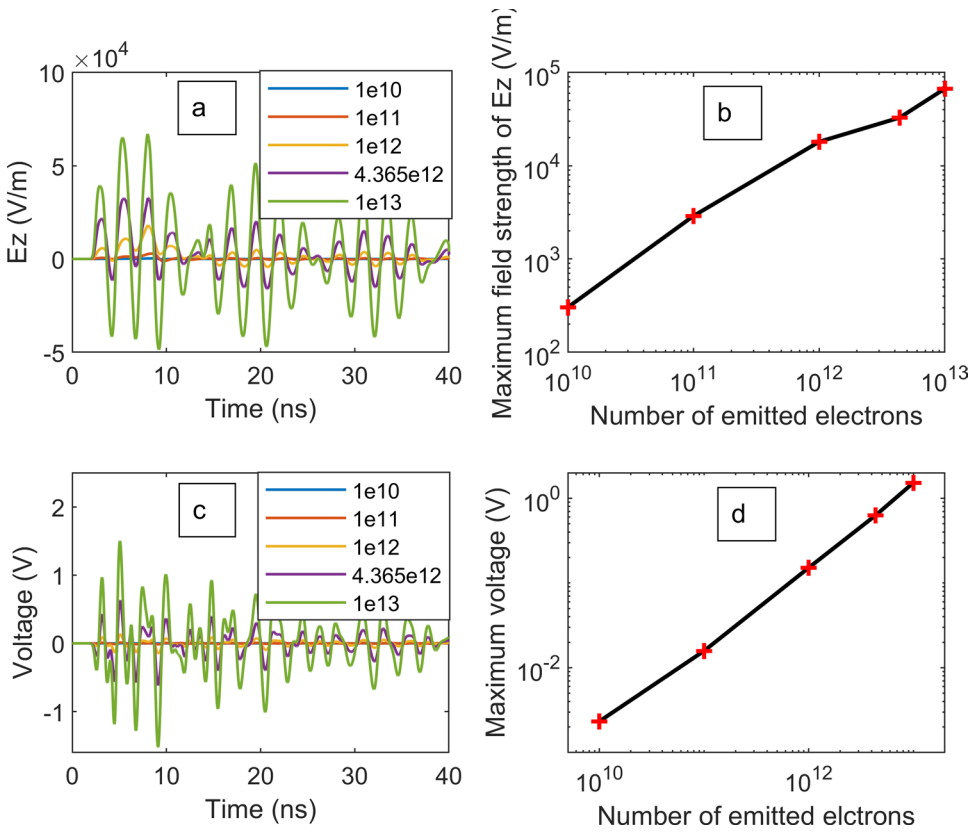

Fig. 7 **a** Time-domain waveform of E_z generated by different numbers of emitted electrons. **b** Relationship between peak amplitude of E_z and number of emitted electrons. **c** Time-domain waveform of V_{iL} generated by different numbers of emitted electrons. **d** Relationship between peak amplitude of V_{iL} and number of emitted electrons

Table 1 Comparison of emission-electron yield

X-ray energy (keV)	Emission-electron yield			
	1-mm Al	1-mm Al+ 50 μm PE	1 mm Al+ 50 μm Epoxy resin	1-mm Al+ 50 μm PTFE
10	1.94×10^{-6}	$< 10^{-7}$	3.0×10^{-7}	4.0×10^{-7}
20	3.31×10^{-4}	1.85×10^{-5}	3.22×10^{-5}	8.40×10^{-5}
30	3.60×10^{-4}	1.81×10^{-5}	3.30×10^{-5}	8.16×10^{-5}
40	3.04×10^{-4}	1.64×10^{-5}	2.57×10^{-5}	7.34×10^{-5}
50	2.29×10^{-4}	1.72×10^{-5}	2.61×10^{-5}	6.14×10^{-5}

coupling voltage increase, which is in line with the expected outcomes [3].

According to the calculation results, the key to reducing coupling interference is to reduce the number of emitted electrons. In practical applications, increasing the thickness or atomic number of the metal cavity (e.g., adding lead shielding outside the cavity) can increase the attenuation of X-rays and reduce the number of electrons emitted. However, this method significantly increases the weight of the entire system and is unsuitable for scenarios with weight requirements. Here, we propose an alternative method. In general, the larger the atomic number of a material, the larger is the cross-section of the photoelectric effect, and more electrons are emitted [31]. Therefore, a layer of a low-Z material (such as polyethylene (PE), $(C_2H_4)_n$) can be attached to the inner side of the metal cavity to reduce the forward electron emission.

Here, we use Monte Carlo calculations to compare the forward electron-emission yields of 1-mm aluminum, 1-mm aluminum with 50 μm PE, 1-mm aluminum with 50 μm epoxy resin ($(C_{11}H_{12}O_3)_n$), and 1-mm aluminum with 50 μm polytetrafluoroethylene (PTFE, $(C_2F_4)_n$) under different energies of X-ray irradiation, as shown in Table 1. Adding even a 50-μm-thick low-Z material can reduce the electron-emission yield by an order of magnitude. Notably, the electron-emission yield is the lowest after adding PE, whereas the electron-emission yield is the highest after adding PTFE because PTFE contains fluorine elements with higher atomic numbers ($Z = 9$). Therefore, this method can be used to reduce the cavity SGEMP and coupling response of the cable.

6 Conclusion

This study uses the three-dimensional FDTD and PIC methods to calculate the cavity SGEMP and solve the cable-terminal voltage response based on the Agrawal transmission-line equation and one-dimensional FDTD method. The cable coupling response inside the metal cavity under X-ray irradiation is analyzed. The calculation results show that in a strong ionizing radiation environment, a strong electromagnetic environment is generated inside the metal cavity. The cable shield terminal load couples with a voltage of 15.32 V, whereas the inner conductor terminal load couples with a voltage of 0.63 V. Under strong X-ray irradiation, the metal cavity cannot provide electromagnetic shielding and introduces new electromagnetic interference. Notably, the cable shield can provide good shielding. If an unshielded cable is placed inside the cavity, the coupling voltage is close to the calculated results for the shielded coaxial cable, which causes greater interference to the devices connected to the cable.

This study also investigated the influence of cable length and cable height on the coupling voltage. The results showed that the longer the cable and the higher it is above the bottom of the cavity, the greater the coupling voltage, and the relationship is approximately linear. The influence of different numbers of emitted electrons on the field strength of the cavity SGEMP and amplitude of the cable coupling voltage was obtained through simulation.

Finally, a method is proposed to reduce the number of emitted electrons by adding low-Z materials, thereby reducing the coupling response. The forward electron-emission yields of 1 mm Al, 1 mm Al + 50 μm PE, 1 mm Al + 50 μm epoxy resin, and 1 mm Al + 50 μm PTFE under different energies of X-ray irradiation were compared through Monte Carlo calculations, verifying the effectiveness of low-Z materials in reducing the number of emitted electrons.

Author contributions All authors contributed to the study conception and design. Material preparation, data collection, and analysis were performed by Mao-Xing Zhang. The first draft of the manuscript was written by Lan-Feng Yuan, and all authors commented on the previous versions of the manuscript. All authors read and approved the final manuscript.

Data availability The data that support the findings of this study are openly available in Science Data Bank at https://cstr.cn/31253.11.sciencedb.j00186.00134 and https://doi.org/10.57760/sciencedb.j00186.00134.

Declarations

Conflict of interest The authors declare that they have no conflict of interest.

References

1. S.S. Wang, Dissertation. Prediction research on shielding effectiveness of electronic equipment box (Harbin University of Science and Technology, 2010). (in Chinese)
2. E.W. Cheng, Y.Z. Chen, W.D. Liu et al., Test method for shielding effectiveness of unmanned aerial vehicle enclosure. High Power Laser Part. Beams (in Chinese) **29**, 55–60 (2017). https://doi.org/10.11884/HPLPB201729.170208
3. Z.Q. Xu, Dissertation. Research on the physical mechanism of electromagnetic pulse excited by the X-ray in the laser ICF facilities (Tsinghua University, 2022). (in Chinese)
4. D. Higgins, K. Lee, L. Marin, System-generated EMP. IEEE Trans. Antennas Propag. **26**, 14–22 (1978). https://doi.org/10.1109/TAP.1978.1141797
5. Z.Q. Xu, C. Meng, Y.S. Jiang et al., 3-D simulation of cavity SGEMP interference generated by pulsed X-rays. IEEE Trans. Nucl. Sci. **67**, 425–433 (2020). https://doi.org/10.1109/TNS.2020.2963983
6. J.G. Wang, L. Liu, S.L. Niu et al., Numerical simulations of environmental parameters of high-altitude nuclear explosion. Mod. Appl. Phys. **14**, 010101 (2023). https://doi.org/10.12061/j.issn.20956223.2023.010101
7. T.A. Tumolillo, J.P. Wondra, MEEC-3D: a computer code for self-consistent solution of the Maxwell–Lorentz equations in three dimensions. IEEE Trans. Nucl. Sci. **24**, 2449–2455 (1977). https://doi.org/10.1109/TNS.1977.4329235
8. R. Holland, A self-consistent two-dimensional EMP code for space-charge limiting and secondary emission. IEEE Trans. Nucl. Sci. **23**, 1927–1932 (1976). https://doi.org/10.1109/TNS.1976.4328601
9. B.L. Beers, D.M. Tasca, J.S. Klisch et al., A methodology for assessing interface threats in satellite electronics from IEMP and cable direct drive excitations. IEEE Trans. Nucl. Sci. **27**, 1579–1584 (1980). https://doi.org/10.1109/TNS.1980.4331072
10. W. Seidler, R. Keyser, D. Walters et al., The limits to hardening electronic boxes to IEMP coupling. IEEE Trans. Nucl. Sci. **29**, 1780–1786 (1982). https://doi.org/10.1109/TNS.1982.4336447
11. J.H. Chen, Dissertation. Study of the SGEMP effect of PCBs exposed in intense X-ray environment (China Academy of Engineering Physics, 2022). (in Chinese)
12. Z.Q. Xu, C. Meng, Y.S. Jiang et al., A code verification for the cavity SGEMP simulation code LASER-SGEMP. IEEE Trans. Nucl. Sci. **68**, 1251–1257 (2021). https://doi.org/10.1109/TNS.2021.3078739
13. J. Allison, K. Amako, J. Apostolakis et al., Geant4 developments and applications. IEEE Trans. Nucl. Sci. **53**, 270–278 (2006). https://doi.org/10.1109/TNS.2006.869826
14. K.S. Yee, Numerical solution of initial boundary value problems involving Maxwell's equations in isotropic media. IEEE Trans. Antennas Propag. **14**, 302–307 (1966). https://doi.org/10.1109/TAP.1966.1138693
15. D.J. John, *Classical Electrodynamics* (Wiley, Hoboken, 1998)
16. F. Liang, Dissertation. Research on efficient hybrid finite-difference time-domain method of coupled transmission lines (Harbin Engineering University, 2020). (in Chinese)
17. O. Buneman, Dissipation of currents in ionized media. Phys. Rev. **115**, 503–517 (1959). https://doi.org/10.1103/PhysRev.115.503
18. J.N. Chen, J.G. Wang, Y.L. Tao et al., Simulation of SGEMP using particle-in-cell method based on conformal technique. IEEE Trans. Nucl. Sci. **66**, 820–826 (2019). https://doi.org/10.1109/TNS.2019.2911933
19. J.N. Chen, J.G. Wang, Z.G. Qiao et al., Study of SGEMP field-coupling inside and outside reentrant cavity. IEEE Trans. Electromagn. Compat. **64**, 1182–1189 (2022). https://doi.org/10.1109/TEMC.2022.3153625
20. J.G. Wang, D.H. Zhang, C.L. Liu et al., UNIPIC code for simulations of high power microwave devices. Phys. Plasmas **16**, 033108 (2009). https://doi.org/10.1063/1.3091931
21. Y. Wang, J.G. Wang, Z.G. Chen et al., Three-dimensional simple conformal symplectic particle-in-cell methods for simulations of high power microwave devices. Comput. Phys. Commun. **205**, 1–12 (2016). https://doi.org/10.1016/i.cpc.2016.03.007
22. F.M. Tesche, M. Ianoz, T. Karlsson, *EMC Analysis Methods and Computational Models* (Wiley, Hoboken, 1996)
23. C.D. Taylor, R.C. Satterwhite, C.W. Harrison, The response of a terminated two-wire transmission line excited by a nonuniform electromagnetic field. IEEE Trans. Antennas **13**, 9872989 (1987). https://doi.org/10.1109/TAP.1965.1138574
24. A.K. Agrawal, H.J. Price, S.H. Gurbaxani, Transient response of multiconductor transmission lines excited by a nonuniform electromagnetic field. IEEE Trans. Electromagn. Compat. **22**, 119–129 (1980). https://doi.org/10.1109/TEMC.1980.303824
25. F. Rachidi, Formulation of the field to transmission line coupling equations in terms of magnetic excitation field. IEEE Trans. Electromagn. Compat. **35**, 404–407 (1993). https://doi.org/10.1109/15.277316
26. H.Y. Xie, J.G. Wang, R.Y. Fan et al., A hybrid FDTD-SPICE method for transmission lines excited by a nonuniform incident wave. IEEE Trans. Electromagn. Compat. **51**, 811–817 (2009). https://doi.org/10.1109/TEMC.2009.2020913
27. C.R. Paul, *Analysis of Multiconductor Transmission Lines* (Wiley, Hoboken, 2007)
28. Z.Q. Xu, C. Meng, P. Wu et al., Simulation of the SGEMP response inside the cavity with aperture. IEEE Trans. Nucl. Sci. **70**, 20–27 (2023). https://doi.org/10.1109/TNS.2022.3213928
29. H.Y. Xie, J.G. Wang, R.Y. Fan et al., SPICE models to analyze radiated and conducted susceptibilities of shielded coaxial cables. IEEE Trans. Electromagn. Compat. **52**, 215–222 (2010). https://doi.org/10.1109/TEMC.2009.2036929
30. H.Y. Xie, Research progress of system level HEMP coupling analysis methods. Mod. Appl. Phys. **14**, 020102 (2023). https://doi.org/10.12061/j.issn.20956223.2023.020102
31. L.J. Tang, Dissertation. Study of electromagnetic interference characteristics of shielded cables based on time-domain BLT equations (Southwest Jiaotong University, 2014). (in Chinese)
32. M.X. Zhang, C. Meng, Z.Q. Xu et al., Cable coupling effect of compound chamber environment in laser inertial confinement fusion driver. Acta Opt. Sin. **42**, 144–153 (2022). (in Chinese)